DESIGN AND ANALYSIS OF A RAYLEIGH SAW RESONATOR FOR GAS DETECTING APPLICATIONS*

V. IONESCU

Department of Physics and Electronics, Ovidius University, Constanta, 900527, Romania,
E-mail: ionescu.vio@gmail.com

Received July 9, 2014

Polymer coated gas-phase sensors using the classical *Rayleigh-type surface acoustic wave* (RSAW) mode showed higher sensitivity and larger dynamic range compared to *bulk acoustic wave* (BAW) sensors, being widely used in a variety of sensor systems for chemical and biological gas detection. Using Comsol Multiphysics software, we investigated a 2D finite element model of a *Surface Acoustic Wave* (SAW) gas sensor, which consists of an *interdigitated transducer* (IDT) etched onto a piezoelectric $LiNbO_3$ substrate and covered with a thin *Poly Isobutylene* (PIB) film. We selected for this study a sensor with two IDT structure types: bi-directional and single phase unidirectional transducer and we computed the deformed shape plot of the resonance and anti-resonance SAW mode. The variation of electrical potential and total displacement as a function of structure depth (y coordinate) was also obtained. The sensor's sensitivity was evaluated by exposing the PIB film to various CH_2Cl_2 (Dichloromethane) concentrations.

Key words: Rayleigh wave, eigenfrequency, IDT electrodes, DCM gas.

1. INTRODUCTION

Typical *surface acoustic wave* SAW gas sensors are composed of a piezoelectric substrate patterned with an *interdigital transducer* (IDT) and a sensitive film on top of the piezoelectric substrate that responds to a specific gas.

A two-port *Rayleigh type surface acoustic wave* (RSAW) resonator coated with a chemo sensitive polymer film makes an excellent high-resolution gas-phase sensor presenting fast response time, excellent overall stability, high sensitivity and low sensor noise [1, 2].

RSAW based gas sensors have found successful application in a variety of industrial implementations such as electronic noses, systems for analysis of chemical and biological gases, medical diagnostics, environmental monitoring and protection, etc. [3–6].

* Paper presented at the 14th International Balkan Workshop on Applied Physics, July 2-4, 2014, Constanta, Romania.

Modern computer-aided design *finite element method* (FEM) techniques implemented in Commercial software like Comsol Multiphysics and ANSYS provide powerful simulation tools for the task of designing SAW gas sensors [7–9]. The use of tools of this type provides an engineer with the ability to develop highly accurate predictions of a system's likely performance, without the need to fabricate a physical prototype [10, 11].

Tsai *et al.* [12] proposed suitable methodology to design SAW sensors working on mass loading principle based on finite element method (FEM) simulation. Wu *et al*. [13] used Taguchi method on FEM results and established robust design processes for SAW sensors based on the mass loading principle.

The RSAW sensor operation principle is fairly simple. If a gas-phase analyte of a certain concentration is applied to its surface, gas molecules are absorbed by the sensing layer until thermodynamic equilibrium is achieved (the number of adsorbed molecules becomes equal to the number of desorbed ones). Due to adsorption, the layer becomes heavier increasing the mass loading on the sensor surface and as a result, the SAW propagation velocity decreases being observed a frequency downshift $\Delta f = f - f_0$ of the sensor resonance, referred to as "sensor signal" [14].

Assuming that the absorbed gas forms an isotropic, non-piezoelectric, non-conducting layer with a thickness of h, a density of ρ on the SAW detector surface, the change in oscillation frequency can be described by [15]:

$$\Delta f = \left(k_1 + k_2\right) f_0^2 \rho h - k_2 f_0^2 \rho h \frac{4\mu}{v_0}\left(\frac{\lambda + \mu}{\lambda + 2\mu}\right) \tag{1}$$

where k_1 and k_2 are the coupling constants determined by the different displacement components of SAW in the substrate; f_0 is the operating frequency without the sensing layer; μ and λ are the shear modulus and Lame constant of the layer; v_0 is the unperturbed velocity of SAW in the piezoelectric substrate.

The first term in Equation (1) represents the frequency change caused by mass loading and the second term depends on the acoustic wave coupled into the layer. Because the layer formed by adsorbed gas is very thin, it can be seen as a simple mass load attached to the surface of the SAW device. Thus Equation (1) can be simplified as:

$$\Delta f = \left(k_1 + k_2\right) f_0^2 \rho h \tag{2}$$

Equation (2) means that the sensor output is proportional to the quantity of the mass loaded on the surface of a SAW device, and it is the theoretical basis for the detection of SAW sensors.

Generally, the sensitivity, S, of a gas sensing device is given by $S = dR/dn$, where R is the device response and n is the gas concentration. A device that develops a higher value of R or a greater frequency shift than other devices for the

same deposited mass possesses a superior sensitivity. The response R for an uncoated substrate is defined as [15]:

$$R = \frac{\Delta \nu}{\nu} = \frac{\Delta f}{f_0} = \left(k_1 + k_2\right) f_0^2 \frac{\Delta m}{A_s} \tag{3}$$

were $\Delta\nu$ is change of the SAW wave velocity after gas absorption and $\Delta m/A_s$ is the mass loading per sensitive surface unit.

The most important parameter for realizing saw gas sensors with low insertion loss and improved device stability is IDT type selection. In this study we performed the analysis of two IDT geometries for a FEM model of a SAW gas sensor: bi-directional and single phase unidirectional transducer (SPUDT), adapted from those proposed by H. Oh *et al*. [16] and presented in fig. 1.

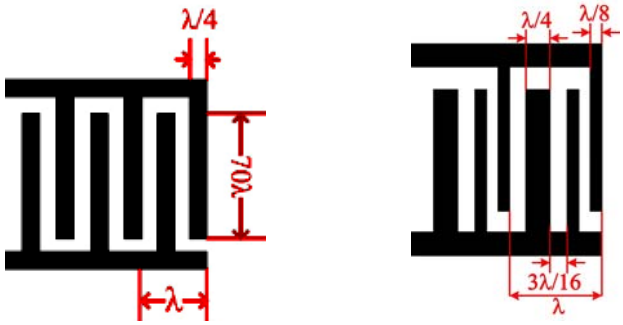

(a) (b)

Fig. 1 – Bi-directional IDT (a) and SPUDT (b) configurations of the SAW strain sensor [16].

2. SIMULATION METHODOLOGY

In this work we have performed FEM simulation of a Rayleigh SAW device using the commercial COMSOL Multiphysics 4.2a software.

Because the geometry of SAW sensor under IDT is periodic, we can model only small part of SAW device and only 2D model is considered, as we can see in fig. 2. Poly Isobutylene (PIB) is used as the chemically resistive sensing layer and YZ-cut $LiNbO_3$ is used as piezoelectric substrate.

The wavelength of the SAW was set to be 4 μm, which is the length of the simulation domain in the propagation direction. The depth of the $LiNbO_3$ substrate was chosen to have 6 wavelengths to limit the size of the simulation. As interdigitated transducers we used aluminum electrodes of λ/4 width and variable height.

The model was set up using the predefined physics interface Piezoelectric Devices and it was used the Plane Strain approximation so that the out-of-plane

strain component was zero. The global displacements (*u; v*) in the *x* and *y* directions and the electric potential (*V)* were computed in a state of plane strain.

In order to model one wavelength of the SAW device, boundary conditions have to enable periodic deformation of the model. These conditions are satisfied by coupling of individual degree of freedom on left and right side of the model. The periodic boundary conditions for both Bidirectional and SPUDT structures set the right (Γ_{R1}, Γ_{R2}) and the left (Γ_{L1}, Γ_{L2}) vertical boundary to have the same displacement and potential. The top boundary Γ_1 is free, and bottom boundary Γ_2 is fixed.

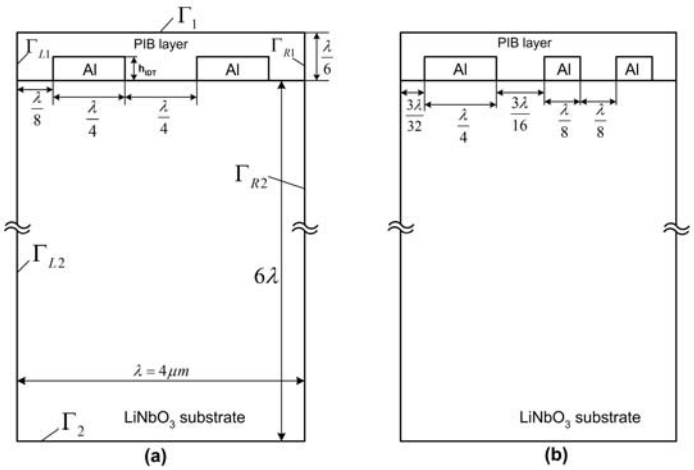

Fig. 2 – 2D unit cell structure employed in the FEM simulation, for bidirectional (a) and SPUDT (b) configurations of a SAW gas sensor.

The elasticity matrix, coupling matrix and relative permittivity values used in the simulation for $LiNbO_3$ substrate were cited in [17]. The Poisson's ratio is taken to be 0.48 and the Young's modulus is set to 10 GPa.

The adsorption of DCM gas is represented as a slight increase of the density of the PIB film. The "partial density" of DCM in the PIB film is then calculated as [18]:

$$\rho_{DCM,PIB} = K \cdot M \cdot c \tag{4}$$

where $K = 10^{1.4821}$ is the air/PIB partition coefficient for DCM, M is its molar mass. DCM concentration in air is given by equation:

$$c = 100 \cdot 10^{-6} \cdot \frac{p}{RT} \tag{5}$$

were p is air pressure (101.325 kPa), T is air temperature (298.15 K) and R is DCM air constant (8.3145 J/mol·K). Any effects of the DCM adsorption on the material properties other than the density are neglected.

Relations between the stress, strain, electric field and electric displacement are established by the following piezoelectric constitutive equations:

$$T = c_E S - e^T E \tag{6}$$

$$D = eS - \varepsilon_S E \tag{7}$$

where T represents the stress matrix, S the strain matrix, E [V/m] the electric field, D the electric displacement matrix [C/m^2], c_E is the elasticity matrix [Pa], e^T is the piezoelectric matrix [C/m^2] and ε_S is the permittivity matrix.

A modal analysis was performed without applying any drive voltage to determine the frequency at which a particular mode resonates for a given wavelength. The solution consists of a set of increasing eigenfrequencies in the specified range that satisfy the applied boundary conditions. The lowest SAW mode will split up in two eigensolutions, the lowest one representing a series resonance, where propagating waves interfere constructively and the other one a parallel ("anti-") resonance, where they interfere destructively. These two frequencies constitute the edges of the stop band, within which no waves can propagate through the IDT.

A harmonic analysis was then realized for this periodic structure around the identified modal frequencies. An alternating voltage was applied on the electrodes to determine the frequency response of the device. For the unit cell structure presented in fig 2.a, the left electrode is grounded and the right one has an input voltage. For the SPUDT structure from fig. 2.b, the central electrode is assigned with a polarization voltage and the other two electrodes from the extremities are grounded.

The central frequency f_0 can be easily obtained analytically from relation:

$$\nu = \lambda \cdot f_0 \tag{8}$$

where ν = 3.488 m·s^{-1} is the SAW propagation velocity in the YZ-cut $LiNbO_3$ piezoelectric layer [19].

3. RESULTS AND DISCUSSIONS

First, a parameter sweep of the electrode height h_{IDT} was done during the frequency dependent study by modifying the electrode parameter from 20 nm to 200 nm at a step size of 20 nm. The results referring to total displacement of the SAW structure along with variation of resonance and anti-resonance frequency were presented in fig. 3. The electrode height h_{IDT} is always represented as a fraction of acoustic wavelength and hence given as a percentage value throughout this paper in the form of normalized electrode height h/λ (%).

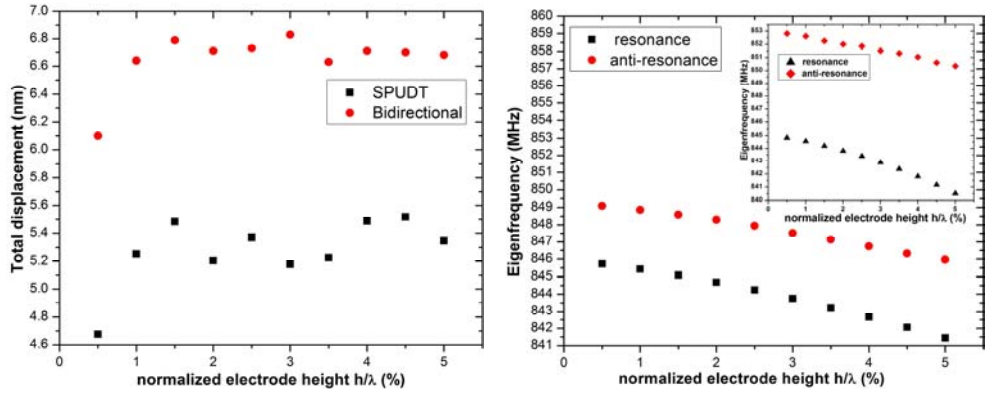

(a) (b)

Fig. 3 – The variation of total displacement of SAW structure with bidirectional and SPUDT electrode configurations (a) and frequency edges of the stop band (b) for the parameter sweep of the electrode height. The inset graph from fig. 3.b represents bidirectional configuration response and the other one is referring to SPUDT geometry.

From fig. 3 we could see that the maximum values for total displacement were 5.518 nm at a resonance frequency of 842.06 MHz for SAW structure A corresponding to SPUDT geometry with h/λ = 4.5 % and 6.833 nm at a resonance frequency of 842.9 MHz for SAW structure B corresponding to bidirectional geometry with h/λ = 3 %. The structures A and B were considered for further investigations.

In Figures 4 and 5 were presented the resonant and anti-resonant SAW modes from the point of view of total displacement and electric potential. Here, the uniform wave traveling the surface along the X direction can be identified from the displacement strength profile.

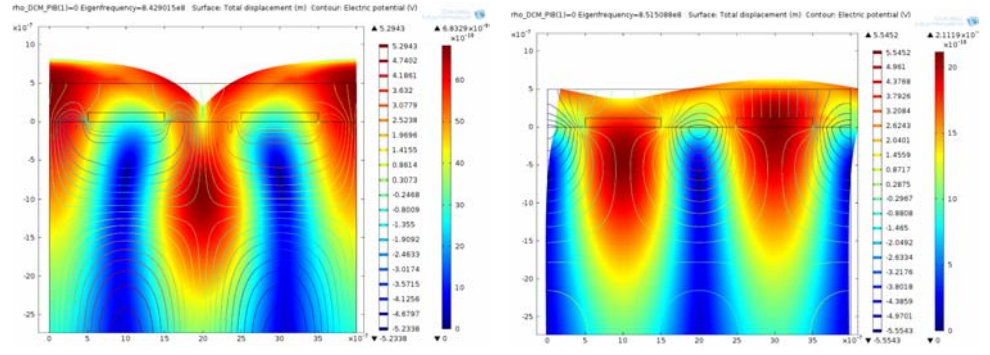

(a) (b)

Fig. 4 – Total displacement (color) and electric potential (contour curve) of SAW structure B with h_{IDT} = 120 nm at: a) resonance frequency (842.9 MHz) and b) anti-resonance frequency (851.51 MHz).

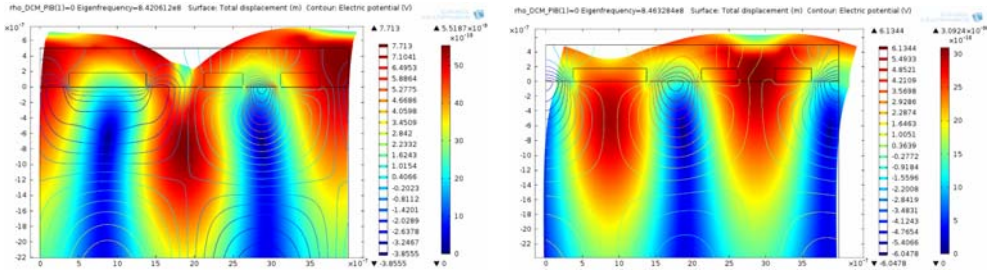

(a) (b)

Fig. 5 – Total displacement (color) and electric potential (contour curve) of SAW structure A with h_{IDT} = 180 nm at: a) resonance frequency (842.9 MHz) and b) anti-resonance frequency (851.51MHz).

Looking in the fig. 4.a at the boundary between $LiNbO_3$ substrate and PIB sensitive film, we could see from the contours line distribution of the electric potential that the negative lines are oriented along the left IDT electrode and the positive ones along the right electrode. In fig. 5.a, the positive potential lines are distributed concentrically between the identical electrodes, along the same boundary.

In figures 4.b and 5.b we observed negative contour lines for electrical potential located at the edges of the substrate-sensitive film interface, the positive ones being distributed along this interface in the space between the two electrodes of structure B and between first two electrodes from the right of structure A.

Total displacement distribution presented in both SAW structures a maximum located at extremities and expanding along the PIB film to the surface of this layer.

As we can see from fig. 6, both the displacements and the electric potential die down within 2 to 3 wavelengths after reaching a maximum within 0.2λ, which is typical for Rayleigh SAW propagation and particle displacements are strictly confined to the sagittal plane [20].

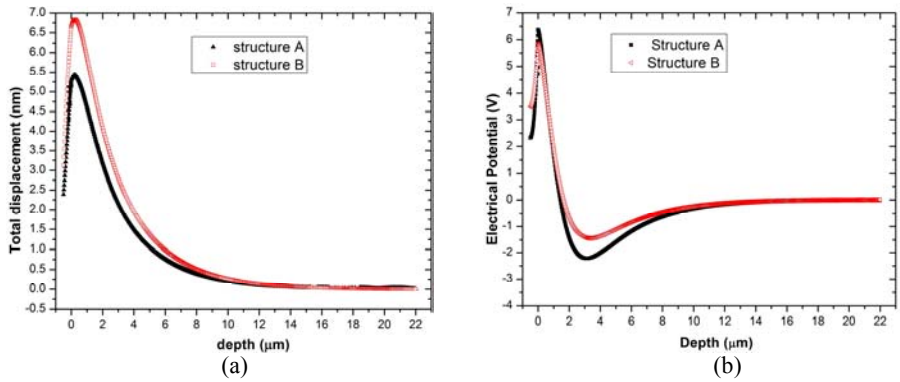

(a) (b)

Fig. 6 – Variation of total displacement (a) and electrical potential (b) for SAW structures A and B at resonance frequency as a function of depth.

From fig. 7 we could see that current density is rising very fast in the SAW structures A and B from a value of about $2.3 \cdot 10^7$ A/m^2 to $4.48 \cdot 10^7$ A/m^2 and $6.11 \cdot 10^7$ A/m^2, respectively, starting from a structure depth of 500 nm to 0 nm; this density has a value of about $0.03 \cdot 10^7$ A/m^2 at 4 wavelengths depth.

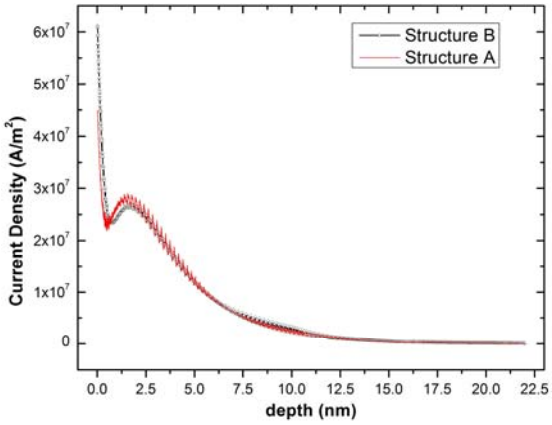

Fig. 7 – Variation of current density for SAW structures A and B at resonance frequency as a function of depth.

The sensitivity of the SAW structures A and B in the form of resonance frequency shift under exposure to Dichloromethane (DCM) gas with concentration varied from 100 ppm to 3000 ppm was shown in Figure 8. The sensitivity curves are linear, with a 2.16 Hz/ppm slope for structure A and 2.3 Hz/ppm slope for structure B.

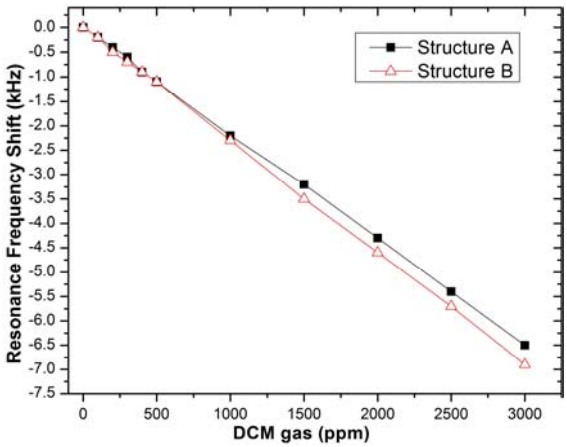

Fig. 8 – Dependence of the resonance frequency shift on the DCM gas concentration for SAW structure A and B.

4. CONCLUSIONS

Two IDT configurations were selected in this paper for FEM analysis of a 2D unit cell model of a SAW gas sensor: bidirectional and single phase unidirectional transducer.

From a parameter sweep variation study of the electrode height h_{IDT} at resonance frequency we choose for further analysis two structures A and B (different in geometry) presenting the maximum displacement at a specific normalized electrode height.

The evolution of total displacement and electrical potential as a function of structure depth confirmed the typical Rayleigh SAW wave propagation in the sensor.

The SAW structure B showed at resonance frequency of 842.9 MHz a maximum displacement of 6.833 nm and a current density of $6.11 \cdot 10^7$ A/m^2 at his surface.

The sensitivity curve for structure B, based on resonance frequency shift, presented a 2.3Hz/ppm slope and we can say that SAW structure with bidirectional electrode geometry had a slightly better sensitivity at a small quantity of DCM gas loaded on the PIB surface.

REFERENCES

1. N. Barie, M. Rapp, H. J. Ache, Sens. Actuat. B Chem. B **46**, 97-103 (1998).
2. F. Bender, L. Waechter, A. Voigt, M. Rapp, *Proceedings of IEEE Sensors Conference*, Toronto, Canada, October 22–24, 2003, 115–119.
3. S. J. Martin, G. C. Frye, J. J. Spates, M. A. Butler, *Proceedings of 1996 IEEE Ultrasonics Symposium*, San Antonio, Texas, November 3-6, 1996, 423-434.
4. M. Rapp, J. Reibel, S. Stier, A. Voigt, J. Bahlo, *Proceedings of the 1997 IEEE International Frequency Control Symposium,* Orlando, Florida*,* May 28-30, 1997, 129–132.
5. E. J. Staples, *Proceedings of 1998 IEEE Ultrasonics Symposium*, Sendai, Japan, October 5-8, 1998, 521-524.
6. T. Wessa, S. Kueppers, G. Mann, M. Rapp, J. Reibel, Organ. Process Res. Dev.**4**, 102–106 (2000).
7. Z. Jurying, C. Tao, C. Yin, *3rd Annual IEEE International Conference on Nano/Micro Engineered and Molecular Systems*, Hainan Island, China, January 6-9, 2008, 1168 – 1171.
8. M.Z. Atashbar, B.J. Bazuin, M. Simpeh, S. Krishnamurthy, Sensors and Actuators B **111-112**, 213-218 (2005).
9. N. Ramakrishnan, A. K. Namdeo, H. B. Nemade, R. P. Palathinkal, Procedia Engineering **41**, 1022–1027 (2012).
10. S. Zhgoon, D. Tsimbal, A. Shvetsov, K. Bhattacharjee, *2008 IEEE International Ultrasonics Symposium (IUS)*, Beijing, China, November 2-5, 1932-1935.
11. G.-S. Chung, D.-T. Phan, Journal of Korean Physical Society **57**, 446-450 (2010).
12. H.-H. Tsai, D. H. Wu, T.-L. Chiang, H. H. Chen, Sensors **9***,* 1394–1408 (2009).
13. D. H. Wu, H. H. Chen, IEEE Transactions on Ultrasonics, Ferroelectrics and Frequency Control **52**, 2403 (2005).
14. K. D. Esmeryan, I. D. Avramov, I. Radeva, Micromachines **3**, 413-426 (2012).
15. H. Wohltjen, *Sens. Actuators* **5**, 307–325 (1984).

16. H. Oh, K. Lee, K. Eun, S.-H. Choa, S. S. Yang, J. Micromech. Microeng. **22**, 1-10 (2012).
17. S. Ahmadi, F. Hassani, C. Korman, M. Rahman, M. Zaghloul, *Proceedings of IEEE Sensors 2004*, Vienna, Austria, October 24-27,2004, 1129–1132.
18. K. H. Clifford, E. R. Lindgren, K. S. Rawlinson, L. K. McGrath, J. L. Wright, Sensors **3**, 236–247 (2003).
19. A. Erko, M. Idir, T. Krist, A. G. Michette, *Modern Developments in X-Ray and Neutron Optics*, Springer-Verlag Berlin Heidelberg New York, 2008.
20. E. Dieulesaint, D. Royer, *Elastic Waves in Solids*, Wiley - Interscience, UK, 1980.